ARMY RESEARCH LABORATORY

Exploiting the Negative Polarization Properties of Indium Gallium Nitride (InGaN)/Gallium Nitride (GaN) Heterostructures to Achieve Frequency Doubled Blue-green Lasers with Deep Ultraviolet (UV) (<250 nm) Emission

by Meredith Reed and Eric D. Readinger

ARL-TR-5228 **June 2010**

NOTICES

Disclaimers

The findings in this report are not to be construed as an official Department of the Army position unless so designated by other authorized documents.

Citation of manufacturer's or trade names does not constitute an official endorsement or approval of the use thereof.

Destroy this report when it is no longer needed. Do not return it to the originator.

Army Research Laboratory
Adelphi, MD 20783-1197

ARL-TR-5228 **June 2010**

Exploiting the Negative Polarization Properties of Indium Gallium Nitride (InGaN)/Gallium Nitride (GaN) Heterostructures to Achieve Frequency Doubled Blue-green Lasers with Deep Ultraviolet (UV) (<250 nm) Emission

Meredith Reed and Eric D. Readinger
Sensors and Electron Devices Directorate, ARL

REPORT DOCUMENTATION PAGE

Form Approved
OMB No. 0704-0188

1. REPORT DATE *(DD-MM-YYYY)*	2. REPORT TYPE	3. DATES COVERED (From - To)
June 2010	DRI	

4. TITLE AND SUBTITLE

Exploiting the Negative Polarization Properties of Indium Gallium Nitride (InGaN)/Gallium Nitride (GaN) Heterostructures to Achieve Frequency Doubled Blue-green Lasers with Deep Ultraviolet (UV) (<250 nm) Emission

5a. CONTRACT NUMBER

5b. GRANT NUMBER

5c. PROGRAM ELEMENT NUMBER

6. AUTHOR(S)

Meredith Reed and Eric D. Readinger

5d. PROJECT NUMBER

5e. TASK NUMBER

5f. WORK UNIT NUMBER

7. PERFORMING ORGANIZATION NAME(S) AND ADDRESS(ES)

U.S. Army Research Laboratory
ATTN: RDRL-SEE-M
2800 Powder Mill Road
Adelphi, MD 20783-1197

8. PERFORMING ORGANIZATION REPORT NUMBER

ARL-TR-5228

9. SPONSORING/MONITORING AGENCY NAME(S) AND ADDRESS(ES)

10. SPONSOR/MONITOR'S ACRONYM(S)

11. SPONSOR/MONITOR'S REPORT NUMBER(S)

12. DISTRIBUTION/AVAILABILITY STATEMENT

Approved for public release; distribution unlimited.

13. SUPPLEMENTARY NOTES

14. ABSTRACT

There is an Army need to develop deep ultraviolet (UV) semiconductor lasers that are compact with a low power budget for use in real-time reagentless biodetection and identification systems as well as water monitoring. Our approach is to develop a visible indium gallium nitride (InGaN) based laser that exploits the negative polarization charge at the heterointerface, which can then be frequency doubled into the deep UV. In the first year of this Director's Research Initiative (DRI), we have developed and tested single heterostructure (SH) *n*-$In_xGa_{1-x}N$/*p*-GaN ("*p*-down") light emitting diodes (LEDs) with 22% In composition and having a peak intensity at 485 nm (blue-green). Under 1% DC, the current injection peaks above 100 A/cm^2, well beyond the current density, 10–25 A/cm^2, at which conventional *p*-up, Ga-polar InGaN/GaN multiple quantum well (MQW) LEDs exhibit significant efficiency droop. The achievement of a blue-green LED with reduced efficiency droop at high current densities is a necessary step for achieving a blue-green laser that uses the benefits of the negative polarization charge.

15. SUBJECT TERMS

III-Nitrides, Semiconductor, GaN, Polarization, Piezoelectric, InGaN, Water Purification and Monitoring, UV

16. SECURITY CLASSIFICATION OF:			17. LIMITATION OF ABSTRACT	18. NUMBER OF PAGES	19a. NAME OF RESPONSIBLE PERSON
a. REPORT	b. ABSTRACT	c. THIS PAGE			Meredith Reed
Unclassified	Unclassified	Unclassified	UU	32	19b. TELEPHONE NUMBER (*Include area code*) (301) 394-0603

Standard Form 298 (Rev. 8/98)
Prescribed by ANSI Std. Z39.18

Contents

List of Figures

1. Statement of the Army Problem

There is an Army need to develop deep ultraviolet (UV) semiconductor lasers that are compact with a low power budget for use in real-time reagentless biodetection and identification systems as well as water monitoring systems that require a laser in the fluorescence free regime (<250 nm) for UV resonance Raman spectroscopy. The Edgewood Chemical and Biological Center (ECBC) has stated a need for deep UV lasers for bio-threat detection systems, and the Tank and Automotive Research, Development and Engineering Center (TARDEC) has expressed a need for these detection systems as well as blue-green lasers for water monitoring and purification systems. At present, deep UV semiconductor lasers have not been realized, with p-type doping and suitable substrate/templates as two areas of research that still require maturation. In addition, blue-green lasers have not been developed due to the detrimental effects of spontaneous and piezoelectric polarization in nitride semiconductors, which leads to efficiency droop at high injection current due to carrier leakage and enhanced Auger recombination in the quantum wells (QWs). The development of high power green lasers will also permit advancement in the high power, high efficiency green light emitting diodes (LEDs) necessary for solid-state lighting solutions for landing beacons and white light illuminators at check points. Therefore, we propose to address both of these needs by exploiting the benefits of negative polarization in indium gallium nitride (InGaN)/gallium nitride (GaN) heterostructures.

2. Objectives

The objective of this research is to explore, develop, and demonstrate the feasibility of exploiting the negative polarization properties of InGaN/GaN heterostructures to achieve frequency doubled blue-green lasers with deep UV (<250 nm) emission.

3. Approach to Achieving the Objectives with Milestones

III-nitride semiconductor lasers in the UV have not been realized due to difficulties associated with the inability to sufficiently *p*-type dope $Al_xGa_{1-x}N$ layers with high aluminum (Al) compositions ($x>0.5$) and the lack of substrates for growth of $Al_xGa_{1-x}N$ active layers. Therefore, the development of an InGaN blue-green laser that can be frequency doubled allows for deep UV lasers that meet current Army needs. However, the path to blue-green high power LEDs and lasers is also difficult given that these devices suffer from efficiency droop at high injection current, which results from polarization charges at the hetero-interface. Typical III-nitride

heterostructure devices are grown along the [0001] direction (Ga-polar) with a p-GaN cap ("*p*-up"), which results in strong built-in electric fields associated with large spontaneous and piezoelectric positive polarization charges at the hetero-interfaces. The positive polarization charge combined with a small conduction band offset in the InGaN/GaN junction leads to a reduced barrier for electron injection, allowing for carrier leakage into the *p*-GaN, while increasing the barrier height for hole injection. To reduce the electron overshoot, an AlGaN electron-blocking layer with a larger bandgap must be used, which increases the polarization field in the quantum well and effectively blocks the injection of holes (*1*). One approach to circumvent these polarization charges and the need for an AlGaN blocking layer is to grow non-polar GaN devices on non-polar substrates (*2, 3*); however, non-polar substrates are very expensive, not well lattice matched, and create difficulties in incorporating the appropriate In content for green emission. However, the positive polarization charges at the hetero-interface of [0001] (In)GaN materials can be ameliorated by reversing the growth sequence of the layers ("*p*-down") or by inverting the polarity (N-polar). This results in a negative polarization charge at the hetero-interface increasing the electron barrier, lowering the hole barrier, and creating a two-dimensional hole gas (2DHG) within the *n*-InGaN. Another approach to create a negative polarization charge at the hetero-interface is to use semi-polar InGaN/GaN devices (*4*). With the advent of thick, *p*-type as-grown GaN templates on sapphire ("*p*-down"), N-polar GaN substrates, and semi-polar (11-22) GaN templates, it is now possible to pursue laser heterostructures that exploit the benefits of negative polarization charges.

3.1 Technical Approach

LEDs form the basis of the most efficient solid-state lighting (SSL) systems available today, but improvements in diode performance are required to develop advanced SSL technologies with a product system efficiency of 50% with lighting that accurately reproduces the sunlight spectrum. Current white light color-mixing based LEDs have a total device efficiency of 30%. One of the main limiting factors for device efficacy is associated with the lack of efficient InGaN or indium aluminum gallium phosphide (InAlGaP)-based LEDs in the wavelength regime from 530 to 580 nm, which are necessary to effectively reproduce the sunlight spectrum. Since no efficient LEDs exist for these wavelengths, this regime is commonly referred to as "the green gap," as seen in figure 1.

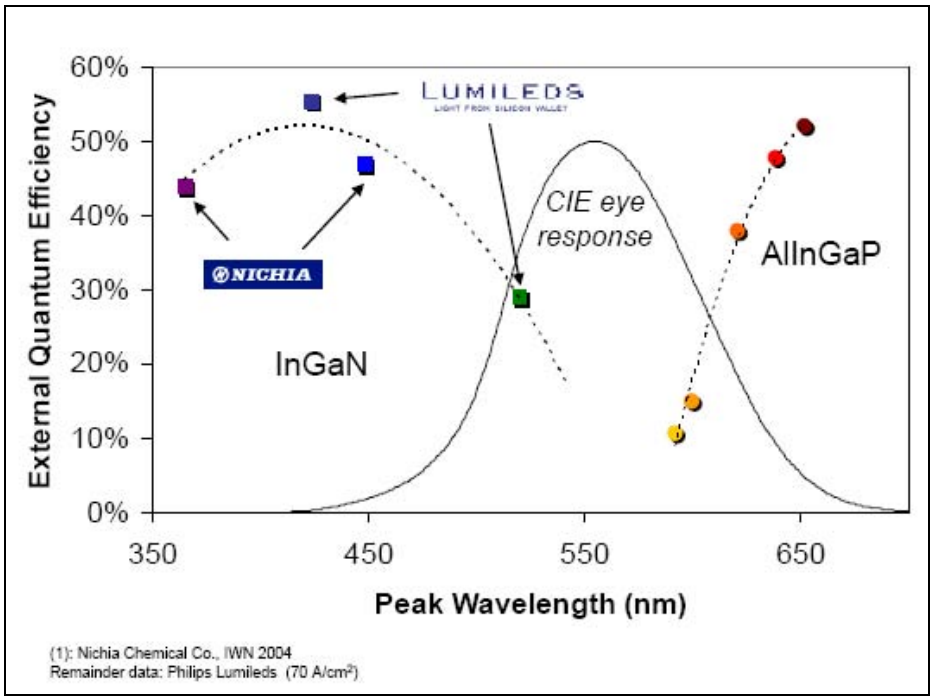

Figure 1. The state-of-the-art external quantum efficiencies of InGaN and AlGaInP devices, based on the Lumileds Luxeon design with 350 mA over a 1×1 mm^2 device (*5*).

In existing conventional multiple quantum well (MQW) devices, InGaN-based LED performance is limited in this spectral regime due to the presence of detrimental positive piezoelectric (PZ) and spontaneous polarization (SP) charge at the hetero-interface, which results in large built-in electric fields within these materials when wurtzite nitride heterostructures are grown along the [0001] direction (*6*–*8*). The presence of the positive PZ and SP charges at the hetero-interface in conventional "*p*-up" devices (figure 2a) has the following detrimental effects:

1. It reduces the barrier for electron confinement, allowing electron overshoot into the *p*-layer; thus requiring the incorporation of a higher bandgap AlGaN electron-blocking layer (EBL).
2. The incorporation of the larger bandgap EBL increases the polarization field in the QW, which impedes hole injection.
3. While the addition of the AlGaN EBL is effective in reducing electron overshoot, it requires high growth temperatures that ultimately compromise the integrity of the InGaN active region. This is especially critical for InGaN-based green LEDs, since these devices are grown at lower temperatures to achieve high In content to achieve green emission.

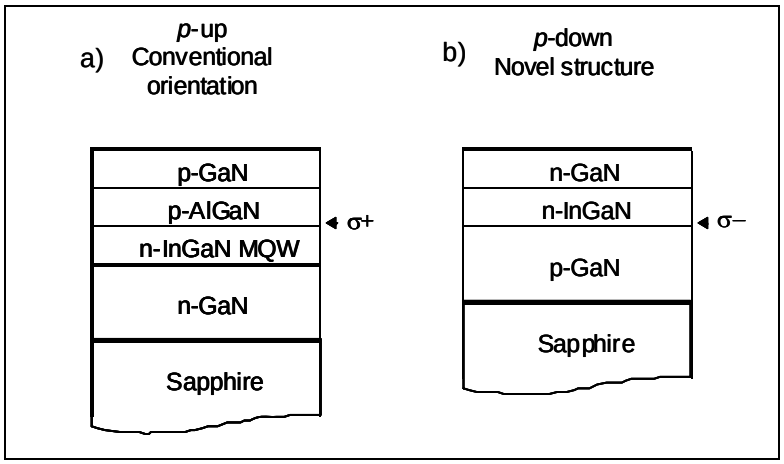

Figure 2. (a) Conventional "*p*-up" LED showing positive polarization charge at the *n*-InGaN/*p*-GaN hetero-interface and (b) a novel "*p*-down" LED showing negative polarization charge at the *n*-InGaN/*p*-GaN hetero-interface.

To circumvent the effects of the polarization charge in LEDs, devices have been grown on non-polar *m*-plane and *a*-plane substrates and on semi-polar substrates, but they have not been fully realized due to the lack of sufficient volume of large area, high quality, lattice-matched non-polar substrates, as well as the difficulty of incorporating high enough In content to shift the wavelength into the green (*9–13*).

For the case of the "*p*-down" Ga-polar devices (figure 2b), a negative polarization charge results at the *n*-InGaN/*p*-GaN interface. Due to the difficulties in fabricating "*p*-down" Ga-polar structures, the utility of employing a negative polarization charge at the *n*-InGaN/*p*-GaN interface has not been widely explored. The effect of the negative polarization charge can be most clearly seen by avoiding additional QWs (*3*) through the study of single or double heterojunction LEDs. The single, thicker active layer of these devices has been shown to be beneficial in achieving higher external quantum efficiency at high injection currents (*10*), with this result attributed to suppression of Auger recombination through lower carrier density for a given current density than can be achieved for QW LEDs (figure 3) (*11*). Such improved performance is essential for applications such as general illumination, projection displays, and automotive headlights.

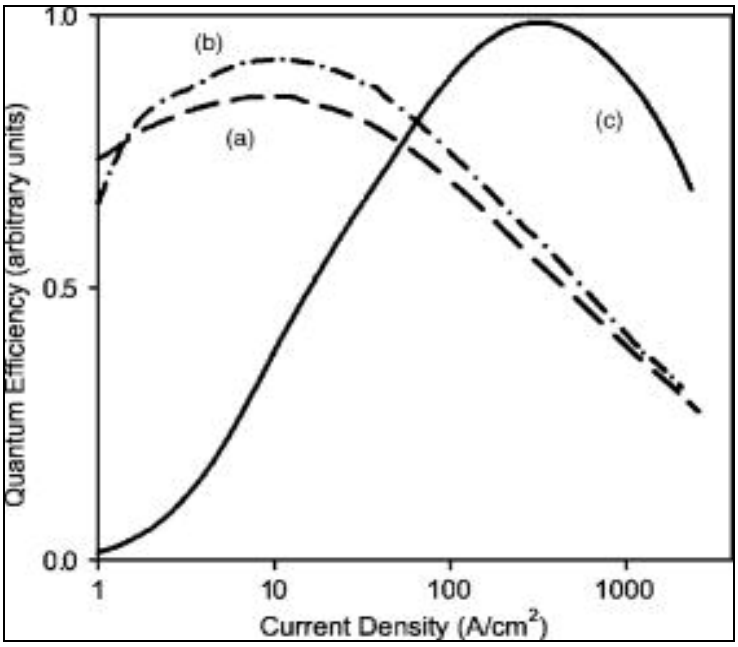

Figure 3. Relative quantum efficiency of (a) two 2.5-nm QWs, (b) six 2.5-nm QWs, and (c) 13-nm double heterostructure (DH) LEDs versus current density (*12*).

With the advent of thick, *p*-type as-grown GaN templates on sapphire and InGaN layers of precisely controllable thickness by metal-organic chemical vapor deposition (MOCVD), it is now possible to pursue single heterostructure (SH) LEDs by employing a technology that may have great potential in commercial applications due to the reduced processing time and cost compared to conventional MOCVD devices (*13, 14*). In this proposal, we plan to optimize the effects of negative polarization charge at the *n*-InGaN/*p*-GaN interface on the performance of a SH *n*-InGaN/*p*-GaN LEDs with "*p*-down" for Ga-polar. We show that the combination of 2DHG formation on the *n*-InGaN side of the hetero-interface and enhancement of the electron barrier to transport across this interface, associated with this negative polarization charge, can reduce efficiency droop while maintaining high current density efficiency without the need for a second hetero-interface or an EBL. The outline for this section is as follows:

1. Modeling and numerical simulations demonstrating the existence and benefits of the negative polarization charge at the *n*-InGaN/*p*-GaN hetero-interface in a "*p*-down" Ga-polar structure
2. Preliminary results of a SH *n*-InGaN/*p*-GaN hetero-interface in a "*p*-down" Ga-polar structure
3. Green laser design and optimization based on the use of the negative polarization charges within this material
4. Frequency double long wavelength laser to achieve deep UV laser for Army applications.

3.2 Theoretical Calculations and Modeling Using an Analytical Solution under Abrupt Approximation

Consider an *n*-type semiconductor with a bandgap of $E_{g,n}$ and a donor concentration of N_D that forms a heterojunction with a *p*-type semiconductor with a bandgap of $E_{g,p}$ and an acceptor concentration of N_A. At the hetero-interface, there is a sheet charge density of σ_{sp+pz} (figure 4). Since the electric field in the neutral regions (far from the junction) must be zero, charge neutrality requires

$$N_D W_n + \sigma_{sp+pz} - N_A W_p = 0\,. \tag{1}$$

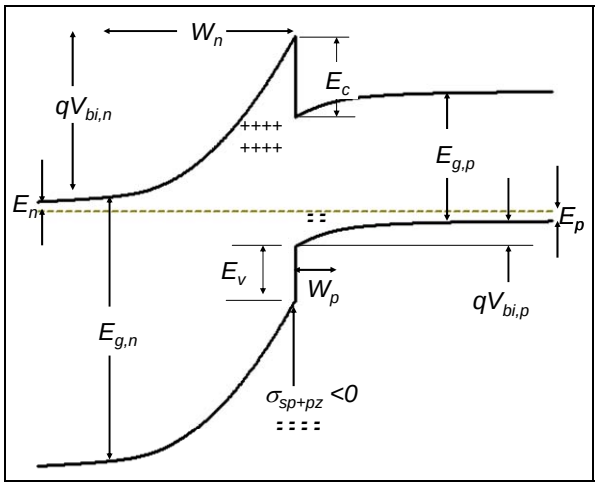

Figure 4. Illustration of the band diagram for a *p-n* heterojunction with a negative polarization charge.

where $W_{n(p)}$ is the depletion width in the *n (p)* region. Under abrupt approximation, the total built-in voltage is given by

$$\frac{qN_D}{2\varepsilon_n} W_n^{\,2} + \frac{qN_A}{2\varepsilon_p} W_p^{\,2} = V_{bi,n} + V_{bi,p} = V_{bi}\,, \tag{2}$$

where $\varepsilon_{n(p)}$ is the dielectric constant for *n-(p-)* type material, q is the electron charge, and

$$qV_{bi} = Q_c E_{g,n} + (1 - Q_c) E_{g,p} - E_n - E_p \tag{3}$$

with Q_c the conduction band offset ratio and $E_{n(p)}$ the conduction (valence) band energy with respect to the Fermi level in the neutral region.

At $\sigma_{sp+pz}=0$, the depletion widths are

$$W_n(0) = \sqrt{\frac{2V_{bi}\varepsilon_n}{qN_D}}\sqrt{\frac{1}{1+k}}$$
$$W_p(0) = \sqrt{\frac{2V_{bi}\varepsilon_p}{qN_A}}\sqrt{\frac{k}{1+k}}, \quad (4)$$

where $k = \frac{N_D}{N_A}\frac{\varepsilon_n}{\varepsilon_p}$. For $\sigma_{sp+pz} \neq 0$,

$$W_n(\sigma_{sp+pz}) = W_n(0)\left[\sqrt{1-\frac{k}{(1+k)^2}\lambda^2} - \frac{k}{1+k}\lambda\right]$$
$$W_p(\sigma_{sp+pz}) = W_p(0)\left[\sqrt{1-\frac{k}{(1+k)^2}\lambda^2} + \frac{1}{1+k}\lambda\right] \quad (5)$$

where $\lambda = \frac{\sigma_{sp+pz}}{N_D W_n(0)} = \frac{\sigma_{sp+pz}}{N_A W_p(0)}$ is the normalized polarization sheet charge density. The band bending in the *n*- and *p*-type material is given by

$$qV_{bi,n}(\sigma_{sp+pz}) = qV_{bi}\frac{1}{1+k}\left[\sqrt{1-\frac{k}{(1+k)^2}\lambda^2} - \frac{k}{1+k}\lambda\right]^2$$
$$qV_{bi,p}(\sigma_{sp+pz}) = qV_{bi}\frac{k}{1+k}\left[\sqrt{1-\frac{k}{(1+k)^2}\lambda^2} + \frac{1}{1+k}\lambda\right]^2 \quad (6)$$

Figure 5 shows the normalized depletion width $W_{n,p}(\sigma_{Sp+pz})/W_{n,p}(0)$ as a function of normalized polarization charge density λ at k=1 and 0.5. Negative interface charge increases (decreases) the depletion width in the *n-(p-)* region with the band bending increasing and decreasing correspondingly. This can be understood from the charge neutrality requirement (equation 1) that negative interface charge requires more positive space charge from the depleted *n*-type layer to compensate, while positive interface charge requires more negative space charge from the depleted *p*-type region to compensate. However, the usable space charge in the *n*- and *p*-layer is limited and thus equations 5–6 are only valid when the limitation is not reached. Since the maximum band bending is limited to the band gap, the maximum positive (negative) space charge per unit area in an *n- (p-)* type material is given by

$$\sigma_{+(-),\max} = \sqrt{\frac{2N_{D(A)}(E_{g,n(p)} - E_{n(p)})\varepsilon_{n(p)}}{q}} \quad (7)$$

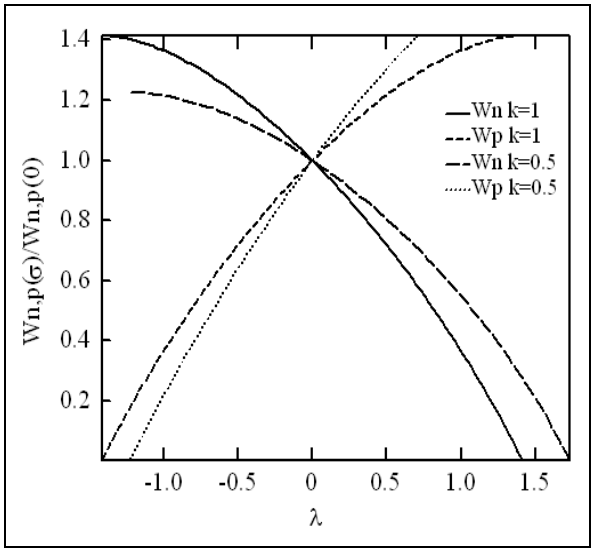

Figure 5. Normalized depletion width as a function of normalized polarization charge density.

Figure 6 shows $\sigma_{+(-),\max}$ as a function of N_D and N_A for GaN.

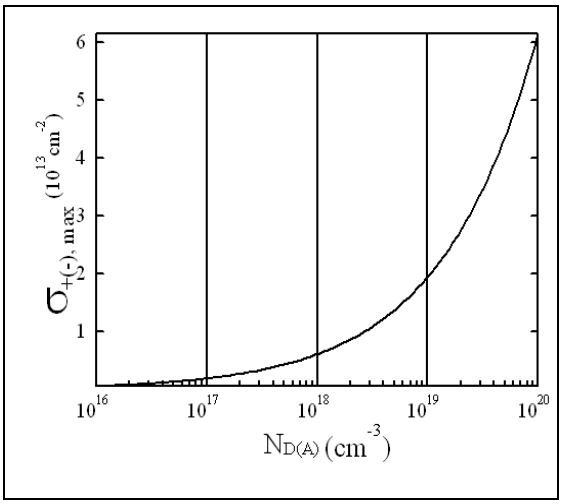

Figure 6. Maximum space charge per unit area as a function of doping concentration in GaN.

In the case where $|\sigma_{sp+pz}| > \sigma_{+(-),\max}$, a two-dimensional electron gas (2DEG) (for $\sigma_{sp+pz}>0$) or 2DHG (for $\sigma_{sp+pz}<0$) forms near the interface to compensate for the excess σ_{sp+pz}. The density of the 2DEG (or 2DHG) is then given by

$$\sigma_{2DEG(2DHG)} = |\sigma_{sp+pz}| - \sigma_{+(-),\max} \tag{8}$$

It is important to point out that the 2DEG (2DHG) always appears near the hetero-interface and in the material with a smaller bandgap. Therefore, the conduction (valence) band offset E_c (E_v) may sometimes become involved in the calculation of maximum space charge, depending on the

band gaps of the two materials. We summarize the results under various conditions in figure 7. We have also included the finite band bending in the 2DEG and 2DHG in the calculation. Neglecting the small difference between the Fermi level and the first confined quantum level and assuming an asymmetric triangle quantum well, we find the band bending in the 2DEG (2DHG) region as

$$E_{2DEG(2DHG)} \approx 2.388\left(\frac{q^2 F_{\max}{}^2 \hbar^2}{2m_{e(h)}}\right)^{1/3} \tag{9}$$

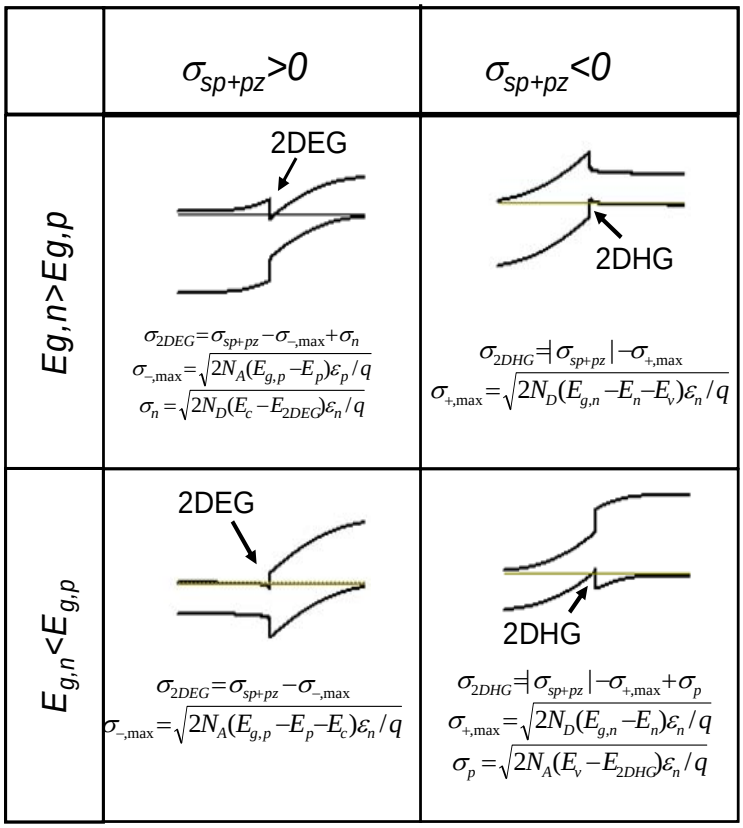

Figure 7. 2DEG and 2DHG in various *p*-*n* hetero-junctions with polarization charge larger than the maximum space charge.

with $F_{\max}$ the electric field corresponding to $\sigma_{+(-),\max}$,

$$F_{\max} = \frac{q\sigma_{+(-),\max}}{\varepsilon_{n(p)}} \tag{10}$$

As an example, we consider two Ga-polar *n*-InGaN/*p*-GaN structures, one is "*p*-up" and the other is "*p*-down". The spontaneous and piezoelectric polarization charge (σ_{sp+pz}) at the InGaN/GaN interface is estimated to be about 1.4×10^{13}e/cm^2 and positive (negative) for "*p*-up" ("*p*-down") Ga-polar structure. The maximum negative depletion charge in the "*p*-up" structure is $\sigma_{-,max}=1.8\times10^{13}$e/cm^2 $>|\sigma_{sp+pz}|$. Therefore, there is no 2DEG in this structure. The calculated

band bending in the *n*-type material is 20% of the total band bending (qV_{bi}), while in a similar structure without polarization charge the band bending in the *n*-region is ~90% of the total band bending. In the "*p*-down" structure, the maximum positive depletion charge is $\sigma_{+,max}=5.7\times10^{12}e/cm^2<|\sigma_{sp+pz}|$. Therefore, a 2DHG forms within the InGaN near the *n*-InGaN/*p*-GaN interface. The calculated 2DHG density is about 1.0×10^{13}e/cm^2, which is in good agreement with the result obtained from a numerical simulation discussed in section 3.3. Almost 100% of the band bending is in the conduction band.

3.3 Numerical Simulation

We have modeled the "*p*-up" and "*p*-down" structure, described previously, by numerically solving the one-dimensional Poisson-Schrödinger equations self-consistently (*11*). We defined a quantum zone sandwiched between two classical zones. We have simulated the electric potential in the quantum zone and extended it continuously to a constant value outside the quantum zone. The total charge is the sum of the ionized doping charges (N^*_D, N^*_A), the free electron and hole charges (n_{free}, p_{free}), the quantum-confined electron and hole charges, and the polarization interface charge:

$$\rho(x) = q[N_D^*(x) - N_A^*(x) - n_{free}(x) + p_{free}(x) - \sum_i n_{c,i}\psi_{c,i}^*(x)\psi_{c,i}(x) + \sum_i n_{v,i}\psi_{v,i}^*(x)\psi_{v,i}(x)n_{V,i} + \sigma_{sp+pz}\delta(x-x_0)] \tag{11}$$

where x_0 is the location of the hetero-interface and $n_{C(V),i}$ is the occupation of the i^{th} electron (hole) sub-band, with its wave-function $\psi_{c(v),i}(x)$ determined by the one dimensional Schrödinger equation:

$$\frac{\hbar^2}{2}\frac{d}{dx}\left(\frac{1}{m_{e(h)}(x)}\frac{d}{dx}\psi_{C(V),i}(x)\right) \pm (E_{C(V)}(x) - E_{C(V),i})\psi_{C(V),i}(x) = 0\,, \tag{12}$$

where $E_{C(V)}(x)$ is the conduction (valence) band profile, $m_{e(h)}$ is the electron (hole) effect mass along the *x* direction, $E_{C(V),i}$ is the energy of the i^{th} confinement electron (hole) sub-band, and the + and – signs are for electrons and holes, respectively. To distinguish quantum confined charge from free charge, a cut-off value is set at the lower potential boundary of the quantum zone. Fermi-Dirac statistics are used for free charges, while the occupation of the confined states is determined by

$$n_{C(V),i} = \frac{m_{e(h)}^{\perp}k_BT}{\pi\hbar^2}\ln\left[1+\exp(\pm\frac{E_F - E_{C(V),i}}{K_BT})\right] \tag{13}$$

where $m_{e(h)}^{\perp}$ is the electron (hole) in-plane effective mass, and the + and – signs are for electrons and holes, respectively.

Displayed in figures 8a and b are the simulated band diagrams at zero bias for "*p*-up" and "*p*-down" structures, respectively. The parameters used in the calculation can be found in reference 16. The inset in figure 8b shows the wave-function of the first confined hole sub-band, its energy and the Fermi energy. The 2DHG density calculated from equation 13 is about 1.0×10^{13} e/cm^2.

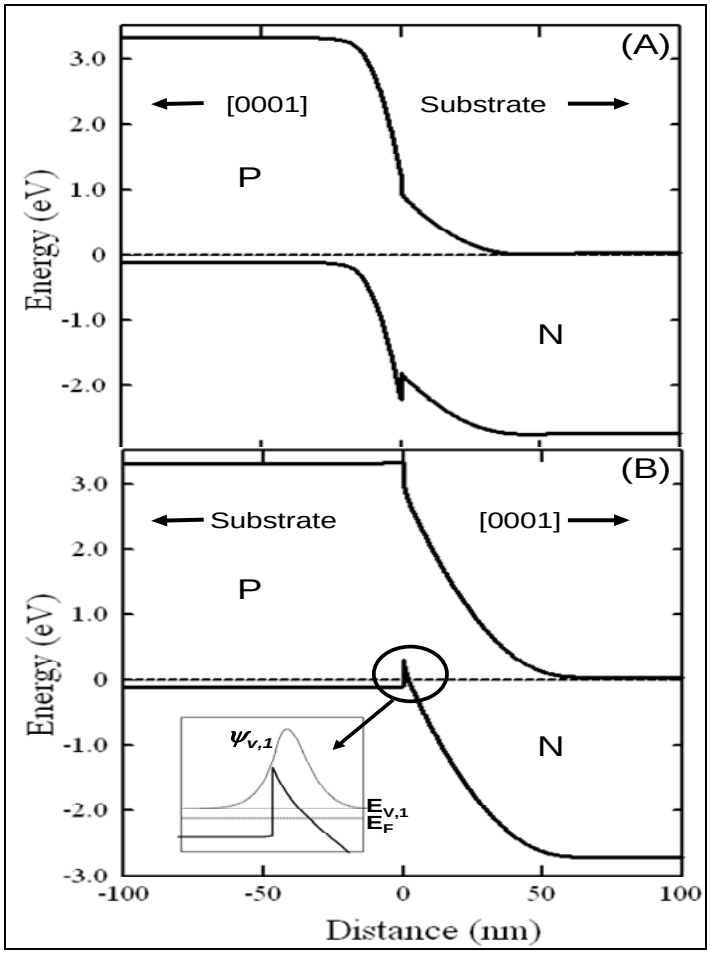

Figure 8. Band diagrams at zero bias for "*p*-up" (a) and "*p*-down" (b) devices. Inset in (b): wave-function of the first confined hole sub-band, its energy and the Fermi energy.

3.4 Results

Figures 9a and b show the band diagrams at a forward current density of 20 A/cm^2 for "*p*-up" and "*p*-down" devices, respectively. Poisson and drift-diffusion current equations with Fermi statistics and thermionic emission at the hetero-junction boundary are solved. The current density and the radiative recombination rate are plotted in figures 10a and b for "*p*-up" and "*p*-down" devices, respectively. In the case of the "*p*-up" device, the positive polarization charge results in a substantially smaller effective electron barrier at the *n*-InGaN/*p*-GaN interface. This leads to a significant leakage of electrons from the active *n*-InGaN to the *p*-GaN layer at room temperature

(figure 9a). About 70% of the electron current overshoots into the *p*-GaN layer, resulting in a significant recombination within this layer (figure 10a). In addition, the injection of holes from the *p*-GaN to the *n*-InGaN experiences a potential barrier spike up to several hundred meV, leading to very inefficient injection of holes into the *n*-InGaN layer (figure 9a). On the other hand, in the "*p*-down" device, the negative polarization charge at the interface leads to a substantially reduced barrier for hole injection from the *p*-GaN to the *n*-InGaN. Here, electrons encounter a significant barrier for injection from the *n*-InGaN into the *p*-GaN, making the *p*-GaN behave like an effective EBL (figure 9b). The formation of the 2DHG in combination with this effective EBL significantly enhances the radiative recombination of injected electrons with 2DHG in the *n*-InGaN active region (figure 10b, dotted line).

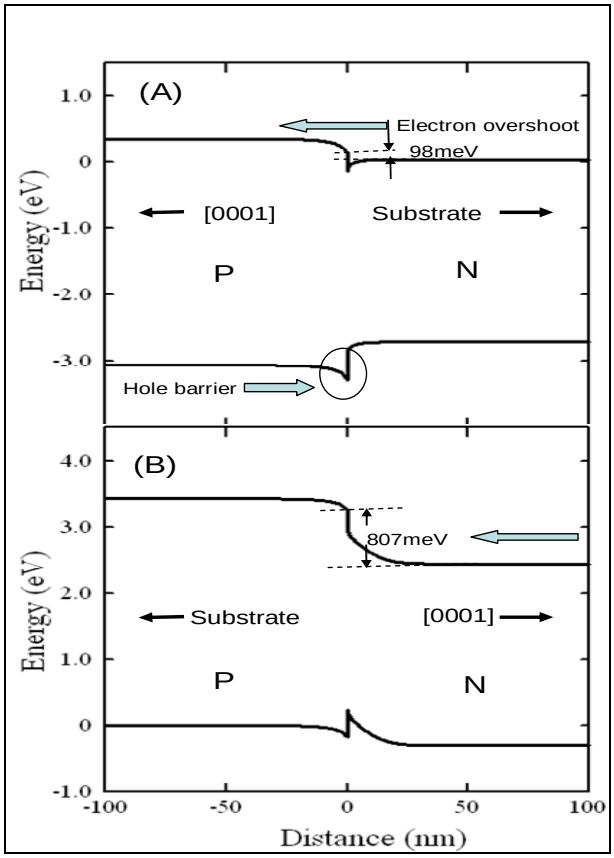

Figure 9. Band diagrams at forward current density of 20 A/cm^2 for "p-up" (a) and "p-down" (b) devices.

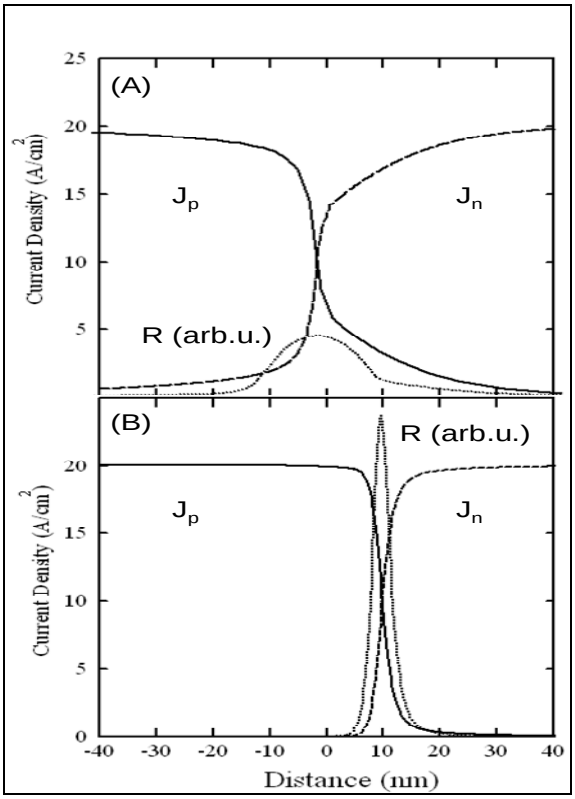

Figure 10. Current density and radiative recombination rate at forward current density of 20 A/cm^2 for "*p*-up" (a) and "*p*-down" (b) devices.

3.5 Preliminary Results

In conjunction with out modeling, SH *n*-InGaN/*p*-GaN structures with *p*-side down were grown on a *p*-GaN template as an initial demonstration and proof of concept (it should be noted that these devices have not been optimized). Single hetero-junction *n*-InGaN/*p*-GaN LED structures comprised of a 0.1–0.2 μm *n*-InGaN (InGaN layer grown at the U.S. Army Research Laboratory [ARL]) layer atop a 5.3-μm *p*-GaN layer on a 2.6-μm *n*-GaN template were grown by hydride vapor phase epitaxy (HVPE) on sapphire substrates at TDI, Inc. Reflectivity and transmission measurements performed using a Perkin Elmer Lambda19 UV/VIS/IR spectrometer system provided a bandgap for the InGaN films and were correlated with x-ray diffraction (XRD) to give In compositions from 7–22%. Mesas were defined using standard reactive ion etching-inductively coupled plasma (RIE-ICP) etching with an etch depth of 0.5 μm to contact the *p*-GaN. Ni/Au *p*-contacts were e-beam evaporated and annealed at 650 °C for 2 min in N_2. Indium titanium oxide (ITO) *n*-contacts were radio frequency (RF) sputtered as the final step in the process. Wafer level current-voltage (I-V) and transfer length measurements (TLM) were performed on the SH LEDs. Details of the device processing may be found elsewhere (*13*). Devices were packaged and electroluminescence measurements were performed using an integrating sphere and an Ocean Optics spectrometer.

Figure 11 shows typical emission spectra and output power at 10% duty cycle (DC) current densities for the *n*-InGaN/*p*-GaN *p*-side down, Ga-polar devices having 22% In composition. At current densities below 25 A/cm^2, the peak emission wavelength rapidly shifts from 502 to 485 nm with a contemporaneous superlinear increase in light output as the injection current increases. At higher injection current densities, a linear increase in power is accompanied by a slower, smaller blue shift to 476 nm by ~85 A/cm^2, with no further blue shift in peak wavelength above this current density. The output power, peak wavelength, and relative external quantum efficiency (EQE) as a function of current density under continuous wave (CW), 1% and 10% DC injection are shown in figure 11b for a wider range of current densities. The light intensity-current (L-I) and EQE curves begin to show saturation at higher current densities for lower DC, and the CW data exhibit a smaller blue shift in the peak wavelength, demonstrating the impact of heating on the device performance. For 1% DC, the peak EQE is attained above 100 A/cm^2, with only about 10% droop up to 500 A/cm^2. Devices of different In content show qualitatively similar behavior.

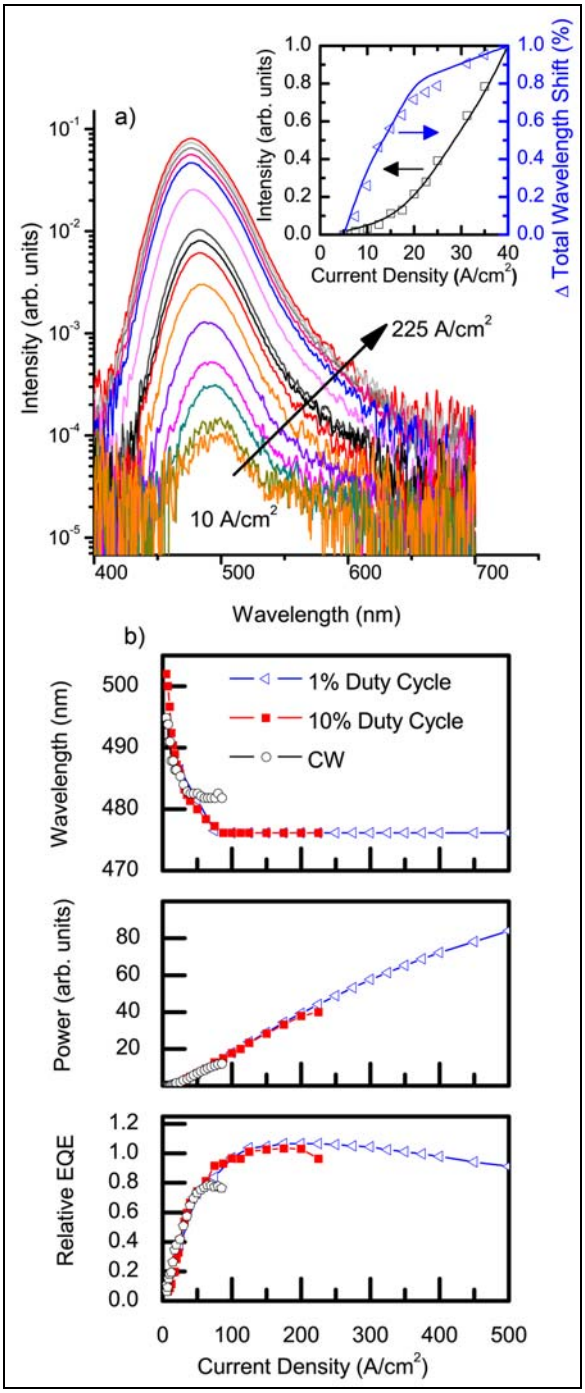

Figure 11. (a) Typical emission spectra at 10% DC current densities for the *n*-InGaN/*p*-GaN *p*-side down, Ga-polar devices having 22% In composition. The inset compares the percent change in total peak wavelength shift and normalized output power at low current density for both predicted (solid line) and measured device behavior (data points). (b) Output power, peak wavelength, and relative EQE as a function of current density for CW, 1% and 10% DC.

Insight into these phenomena may be gleaned from comparison of the modeling of *p*-up and *p*-down Ga-polar devices at forward current density of 25 A/cm^2 using a self-consistent solution of the Poisson-Schrödinger equations that includes drift-diffusion currents, Fermi statistics, and thermionic emission at the heterojunction boundary (figure 12). Accounting for spontaneous and piezoelectric polarizations, the total charge at the InGaN/GaN interface is estimated to be ~10^{13} e/cm^2 and negative (positive) for *p*-down (*p*-up), Ga-polar structures. This negative polarization charge is greater than the maximum positive space charge that the *n*-InGaN layer can support, Thus, in the case of the *p*-down, Ga-polar device, the negative polarization charge at the interface leads to the formation of a well-confined 2DHG just within the InGaN near the *n*-InGaN/*p*-GaN interface, a substantially reduced barrier for hole injection from the *p*-GaN to the *n*-InGaN, and a significantly enhanced conduction band heterobarrier that acts as an effective blocking layer for electron transport to the *p*-GaN (figure 12a).

In contrast, the positive polarization charge at the hetero-interface in the conventional *p*-up geometry causes a dramatic reduction in the conduction band barrier to electron transport into the *p*-GaN, as well as a steep (up to several hundred meV) barrier to hole transport into the *n*-InGaN (figure 12c). It could also lead to the formation of a 2DEG within the InGaN near the hetero-interface. The impact of these contrasting band diagrams on electron and hole current densities and radiative recombination rates in these device structures is shown in figures 12b and d. For the *p*-down device, the formation of the 2DHG and reduction in the barrier to hole injection in the *n*-InGaN, in combination with the effective electron confinement in the same layer due to the higher conduction band hetero-barrier, significantly enhance the radiative recombination of electrons with holes in the *n*-InGaN active region, as shown in figure 12b by the dotted line. The simultaneous rapid blue shift and superlinear increase in electroluminescence observed in figure 12a 25 A/cm^2 are consistent with radiative tunneling, as described for GaAs *p*-*n* junctions (*19*). Under forward bias, some of the injected electrons undergo spatially indirect recombination with the 2DHG. With increasing forward bias, the electron quasi-Fermi level increases, leading to more high energy electrons recombining with the 2DHG and a concomitant blue shift of the electroluminescence. This effect, in combination with the improved overlap of electron and hole wave-functions, results in a superlinear increase in light output.

The inset of figure 12a shows good agreement between modeling and device behavior at low current densities. The more linear increase in intensity accompanied by a slower, smaller blue shift in peak wavelength at higher current density is attributed to a transition to direct recombination, as predicted by our modeling, and residual band filling effects possibly associated with compositional inhomogeneity in the high In content *n*-InGaN. The low current density behavior, characteristic of the *p*-down SH device, is distinctly different from band filling in conventional DH LEDs, for which the electroluminescence (EL) peak is nearly stationary at low injection levels, but exhibits a larger blue shift for high injection (*20*). The blue shift is also different from the blue shift in QW structures due to the quantum confined Stark effect, in which the majority of the contribution to the blue shift is from the Stark shift of the hole band.

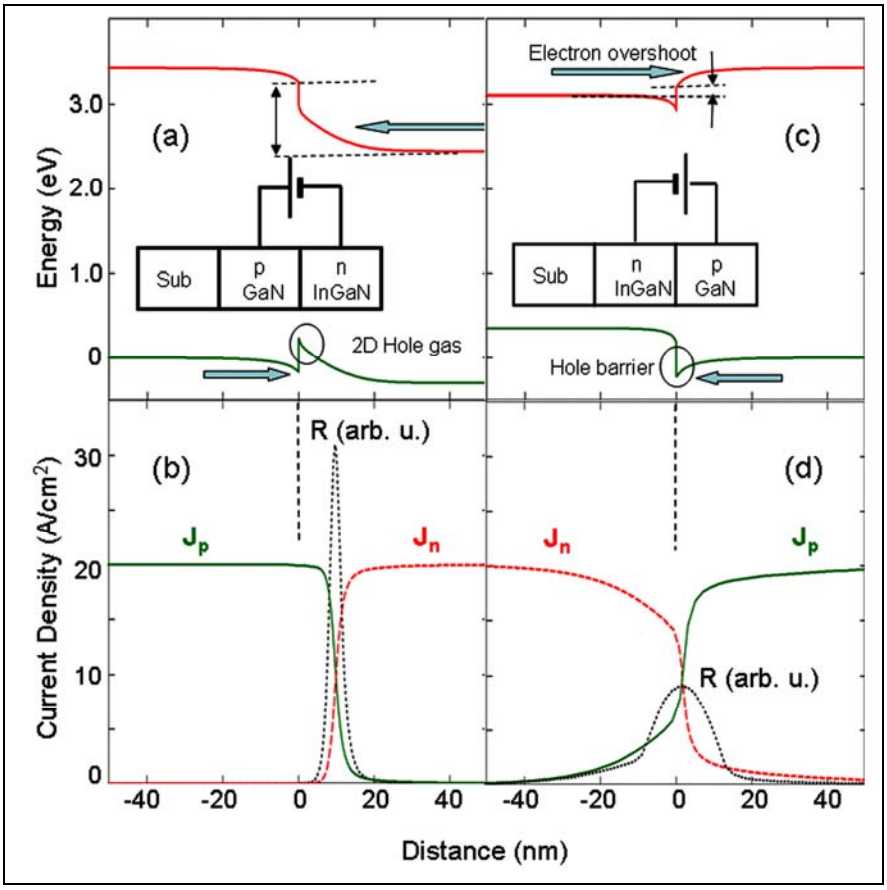

Figure 12. Simulations of band structures and resulting current density distributions and radiative recombination rates at 20 A/cm^2 for *p*-up and *p*-down *n*-InGaN/*p*-GaN Ga-polar SH LEDs: (a) band diagram and (b) electron (solid line) and hole (dashed) current density distributions and radiative recombination rate (dotted line) of *p*-down device; and (c) band diagram and (d) electron (solid line) and hole (dashed) current density distributions and radiative recombination rate (dotted line) of *p*-up device.

In the case of the conventional *p*-up Ga-polar structure, the substantially smaller effective electron barrier at the *n*-InGaN/*p*-GaN interface leads to a significant leakage of electrons from the active *n*-InGaN to the *p*-GaN layer, resulting in recombination within the *p*-GaN layer, as shown in figure 12d, and characteristic blue emission (*21*) from fabricated devices (not shown). In addition, the high potential barrier to hole injection into the *n*-InGaN leads to very inefficient injection of holes into the *n*-InGaN layer. The first practical devices (*22*) showed that these issues are partially remedied through insertion of a wider bandgap AlGaN EBL at the hetero-interface that aids electron confinement in the active region in conventional InGaN/GaN MQW and DH LEDs.

The EQE of the *p*-down SH *n*-InGaN/*p*-GaN LED under 1% DC current injection peaks above 100 A/cm^2, well beyond the current density (~10 to 25 A/cm^2) at which conventional *p*-up, Ga-polar InGaN/GaN MQW LEDs already exhibit significant efficiency droop (*8, 15*). It has been

suggested that the peak efficiency at low current density in conventional InGaN/GaN MQW LEDs is strongly dependent upon electron leakage from the active region (*4*) and device defect density (*19*), while the drop in efficiency at high current density has been attributed to Auger recombination resulting from the high QW carrier density (*15, 16*), although electron leakage may still play a role (*8, 23*). While the efficiency at low current density in our *p*-down SH LED is limited by its tunneling behavior, the efficiency at high current density should strongly depend on the effective width for radiative recombination within the triangular potential that confines the 2DHG. Since the electron wave function is not confined, for comparison purposes this effective width can be defined as that of an equivalent InGaN/GaN QW with a similar hole wave function as that in our LED under forward bias. This width is ~12 nm, suggesting that our EQE should peak at higher current densities because of the reduced carrier density in this active region. A 430-nm DH LED with similar active region width (13 nm) has been reported to have peak EQE at current density beyond 200 A/cm^2 (*15*). The lack of significant efficiency droop in our *p*-down SH LED at 1% DC current densities as high as 500 A/cm^2 without need of the AlGaN electron blocking layer or the second heterojunction to ensure hole confinement required in conventional *p*-up Ga-polar DH LEDs shows promise for simplified LED structures with lower manufacturing costs.

In summary, single heterojunction *n*-InGaN/*p*-GaN LEDs with "*p*-down" Ga-polar have been grown on HVPE *p*-GaN templates. The large negative interface charge for Ga polarity has been exploited for improved hole injection and electron and hole confinement in the *n*-InGaN, leading to peak EQE at current densities far beyond those at which conventional MQW LEDs exhibit efficiency droop. The lack of significant efficiency droop in our devices at pulsed current densities up to 500 A/cm^2 shows promise for high current density applications.

4. Conclusions

To date, for our FY09 Director's Research Initiative (DRI) (Year 1 results), we have grown and characterized bulk InGaN epilayers with a compositional range up to 33% In for application as *n*-InGaN active regions on various substrates. We fabricated SH *n*-$In_xGa_{1-x}N$/*p*-GaN ("*p*-down") LED structures grown on sapphire substrates with In compositions varied from $0.07<x<0.33$. Standard device processing techniques created a mesa in the 0.1–0.2 μm thick InGaN active layer, which defined the device's active area. The devices were diced, mounted on TO-39 headers and tested for output power and wavelength as a function of current density. Figure 13 shows the typical emission spectra and output power at 10% duty cycle current densities for a Ga-polar *p*-down SH with 22% In composition, having a peak intensity at 485 nm (blue-green).

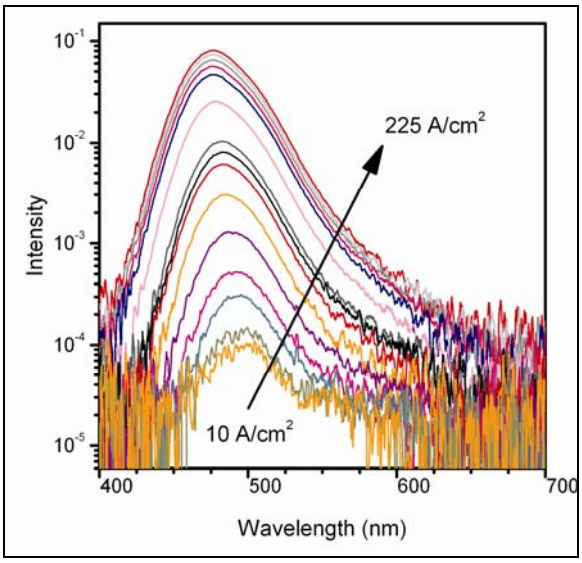

Figure 13. The typical emission spectra at 10% DC with respect to current density for an *n*-$In_{0.22}GaN$/*p*-GaN *p*-down, Ga-polar device.

The EQE of this device as a function of DC is shown in figure 14. Under 1% DC, the current injection peaks above 100 A/cm^2, well beyond the current density 10–25 A/cm^2 at which conventional *p*-up, Ga-polar InGaN/GaN MQW LEDs exhibit significant efficiency droop (*1*). The achievement of a blue-green LED with reduced efficiency droop at high current densities satisfies our Q4 milestone for Year 1 and is a necessary step for achieving a blue-green laser that uses the benefits of the negative polarization charge.

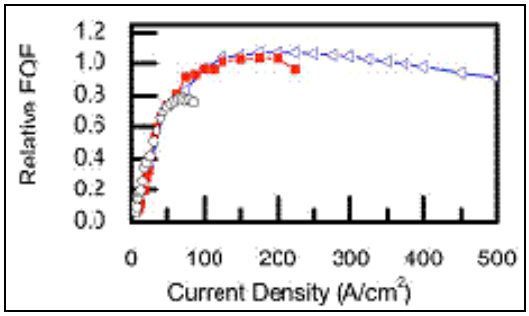

Figure 14. The relative EQE as a function of current density for cw (circles), 1% (triangles) and 10% (squares) DC.

To date, the FY09 DRI has resulted in two conference presentations and papers at the Conference on Lasers and Electro-Optics; two invited conference presentations at the International Symposium on Semiconductor Light Emitting Devices and 216th Electrochemical Society Symposium; two invited journal publications at *Physica Status Solidi* and *Electrochemical Transactions*; one journal publication in the *Applied Physics Journal* (*24*); and one filed patent.

5. References

1. Kim, M.; Schubert, M. F.; Dai, Q.; Kim, J. K.; Schubert, E. F.; Piprek, J.; Park, Y. *Appl. Phys. Lett.* **2007**, *91*, 183507.
2. Craven, M. D.; Waltereit, P.; Speck, J. S.; DenBaars, S. P. *Appl. Phys. Lett.* **2004**, *84*, 496.
3. Ng, H. M. *Appl. Phys. Lett.* **2002**, *80*, 4369.
4. Shen, H.; Wraback, M.; Zhong, H.; Tyagi, A.; DenBaars, S. P.; Nakamura, S.; Speck, J. S. to be published in *Appl. Phys. Lett.*
5. Goetz, W. Philips Lumileds Lighting Company Inc, www.lumileds.com (accessed 2009).
6. Bykhovski, A.; Gelmont, B.; Shur, M. *J. Appl. Phys.* **1993**, *74*, 6734.
7. Takeuchi, T.; Sota, S.; Katsuragawa, M.; Komori, M.; Takeuchi, H.; Amano, H.; Akasaki, I. *Jpn. J. Appl. Phys.* **1997**, Part 2, 36, L382.
8. Kozodov, P.; Hansen, M.; DenBaars, S. P.; Mishra, U. K. *Appl. Phys. Lett.* **1999**, *74*, 3681.
9. Iso, K.; Yamada, H.; Hirasawa, H.; Fellows, N.; Saito, M.; Fujito, K.; DenBaars, S. P.; Speck, J. S.; Nakamura, S. *Jpn. J. App. Phys.* **2007**, *46* (40), L960–L962.
10. Craven, M. D.; Waltereit, P.; Speck, J. S.; DenBaars, S. P. *Appl. Phys. Lett.* **2004**, *84*, 496.
11. Ng, H. M. *Appl. Phys. Lett.* **2002**, *80*, 4369.
12. Gardner, N. F.; Mueller, G. O.; Shen, Y. C.; Chen, G.; Watanabe, S.; Goetz, W.; Krames, M. R. *Appl. Phys. Lett.* **2007**, *91*, 243506.
13. Waltereit, P.; Brandt, O.; Trampert, A.; Grahn, H. T.; Menniger, J.; Ramsteiner, M.; Reiche, M.; Ploog, K. H. *Nature* **2000**, *406*, 865.
14. Shen, Y. C.; Mueller, G. O.; Watanabe, S.; Gardner, N. F.; Munkholm, A.; Krames, M. R. *Appl. Phys. Lett.* **2007**, *91*, 141101.
15. Zhang, Y.; Singh, J. *J. Appl. Phys.* **1998**, *85*, 587.
16. Vurgaftman, I.; Meyer, J. *Appl. Phys. Rev.* **2003**, *94*, 3675.
17. Reed, M. L.; Readinger, E. D.; Shen, P.; Wraback, M.; Syrkin, A.; Usikov, A.; Dmitriev, V. *Electrochem. Soc. Tran* **2007**, *11* (5) 171–174.
18. Zywietz, T.; Neugebauer, J.; Scheffler, M. *Appl. Phys. Lett.* **1998**, *73*, 487.
19. Zywietz, T.; Neugebauer, J.; Scheffler, M. *Appl. Phys. Lett.* **1999**, *74*, 1695.

20. Sumiya, M.; Yoshimura, K.; Ito, T.; Ohtsuka, K.; Fuke, S.; Mizuno, K.; Yoshimoto, M.; Koinuma, H.; Ohtomo, A.; Kawasaki, M. *J. Appl. Phys.* **2000**, *88*, 1158.

21. Collazo, R.; Mita, S.; Aleksov, A.; Schlesser, R.; Sitar, Z. *J. Cryst. Growth* **2006**, *287*, 586.

22. Monroy, E.; Sarigiannidou, E.; Fossard, F.; Gogneau, N.; Bellet-Amalric, E.; Rouvière, J.-L.; Monnoye, S.; Mank, H.; Daudin, B. *Appl. Phys. Lett.* **2004**, *84*, 3684.

23. Macht, L.; Weyher, J. L.; Hageman, P. R.; Zielinski, M.; Larsen, P. K. *J. Phys. Condens. Matter* **2002**, *14*, 13345.

24. Reed, M. L.; Readinger, E. D.; Shen, H.; Wraback, M.; Syrkin, A.; Usikov, A.; Kovalenkov, O. V.; Dmitriev, V. A. *Appl. Phys. Lett.* **2008**, *93*, 133505.

6. Transitions

The LED portion of this work is being funded through a Department of Energy (DOE) program to address the “green” gap problem, $1.8M over 3 years. The development of a frequency doubled laser into the deep UV will have immediate applications in communications, water purification and monitoring, and bio-threat sensing.

List of Symbols, Abbreviations, and Acronyms

2DEG	two-dimensional electron gas
2DHG	two-dimensional hole gas
Al	aluminum
ARL	U.S. Army Research Laboratory
CW	continuous wave
DC	duty cycle
DH	double heterostructure
DRI	Director's Research Initiative
EBL	electron-blocking layer
ECBC	Edgewood Chemical and Biological Center
EL	electroluminescence
EQE	external quantum efficiency
GaN	gallium nitride
HVPE	hydride vapor phase epitaxy
InAlGaP	indium aluminum gallium phosphide
InGaN	indium gallium nitride
ITO	indium titanium oxide
I-V	current-voltage
LEDs	light emitting diodes
L-I	light intensity-current
MOCVD	metal-organic chemical vapor deposition
MQW	multiple quantum well
PZ	positive piezoelectric
QW	quantum well

RF	radio frequency
RIE-ICP	reactive ion etching-inductively coupled plasma
SH	single heterostructure
SP	spontaneous polarization
SSL	solid-state lighting
TARDEC	Tank and Automotive Research, Development and Engineering Center
TLM	transfer length measurements
UV	ultraviolet
XRD	x-ray diffraction

No. of Copies	Organization
1 ELEC	ADMNSTR DEFNS TECHL INFO CTR ATTN DTIC OCP 8725 JOHN J KINGMAN RD STE 0944 FT BELVOIR VA 22060-6218
1 CD	US ARMY RSRCH LAB ATTN RDRL CIM G T LANDFRIED BLDG 4600 ABERDEEN PROVING GROUND MD 21005-5066
3 CDS	US ARMY RSRCH LAB ATTN IMNE ALC HRR MAIL & RECORDS MGMT ATTN RDRL CIM L TECHL LIB ATTN RDRL CIM P TECHL PUB ADELPHI MD 20783-1197
1 CD	US ARMY RSRCH LAB ATTN DR MEREDITH L REED 2800 POWDER MILL RD ADELPHI, MD 20783

TOTAL: 6 (1 ELEC, 5 CDS)

INTENTIONALLY LEFT BLANK.